Using electron density to predict synthon formation in a 4-hydroxybenzoic acid : 4,4′-bipyridine co-crystal†

Jonathan J. Du[1], Stephen A. Stanton[1], Peter A. Williams[1,4], Jennifer A. Ong[1], Paul W. Groundwater[1], Jacob Overgaard[3], James A. Platts[2] and David E. Hibbs[1]*

[1]*Faculty of Pharmacy, University of Sydney, NSW 2006 Australia*

[2]*School of Chemistry, Cardiff University, Cardiff, CF10 3AT, UK*

[3]*Department of Chemistry, Center for Materials Crystallography, Aarhus University, Langelandsgade 140, Aarhus C, 8000, Denmark*

[4]*School of Science and Health, Western Sydney University, Locked Bag 1797, Penrith, NSW 2751*

**Corresponding author: David E. Hibbs,* david.hibbs@sydney.edu.au

†Electronic supplementary information (ES) available. CCDC 1562101, 1562102 and 1562103. For ESI and crystallographic data in CIF or other electronic formats, see DOI: XXXXXXX

Abstract

Experimental charge density distribution studies complemented by quantum mechanical theoretical calculations of 4-hydroxybenzoic acid (4HBA) (**1**), 4,4′-bipyridine (44BP) (**2**) and one polymorphic form of the co-crystal containing 4HBA and 44BP molecules in a 2:1 ratio (**3**), have been carried out *via* high resolution single-crystal X-ray diffraction. Synthon formation was found to be the main driving force for crystallisation in both (**1**) and (**3**) with a carboxylic acid homosynthon present in (**1**) and a heterosynthon in (**3**) comprised of a carboxylic acid from 4HBA and a pyridine nitrogen and aromatic hydrogen from 44BP. Topological analysis revealed the bonding in the homosynthon to be stronger than the heterosynthon (305.88 *versus*. 193.95 kJ mol^{-1}) with a greater number of weak interactions in (**3**) helping to stabilise the structure. The distance from the hydrogen and hydrogen bond acceptor to the bond critical point (bcp) was also found to be a significant factor in determining bond strength, potentially having a greater effect than lone pair directionality. Two different methods of lattice energy calculations were carried out and both methods found (**1**) to be more stable than (**3**) by ~40 and 10 $kJmol^{-1}$ for the LATEN and PIXEL methods respectively. Energy framework diagrams reveal (**1**) to be dominated by coulombic forces while both coulombic and dispersion forces are prominent in (**3**) contributing equally to the lattice energy. This study examined the utility of homosynthons and heterosynthons in future crystal engineering endeavours and concluded that although in this case the single molecule crystal was more thermodynamically stable, the asymmetry of the co-crystal system allowed it to form a wider range of interactions resulting in only a small reduction in stability. This highlights the potential of using heterosynthons to develop co-crystals to improve pharmaceuticals. These findings highlight the utility of high resolution single crystal X-ray crystallography in rationalising observed physical properties.

Introduction

The utility of co-crystals in crystal engineering specifically for improving active pharmaceutical ingredients (APIs) has recently refocussed the scientific spotlight onto the field of crystallography. Co-crystals are defined by Springuel *et al*. as "a crystal composed of at least two components (here API and co-crystal former (or co-former)) that are solid at room temperature"[1]. These have emerged as a viable alternative to formulate potential pharmaceuticals into suitable dosage forms, particularly important when over 90% of potential drugs do not progress past initial clinical trials due to poor physicochemical properties such as solubility, stability and bioavailability[2]. Co-crystals have the additional benefit of modulating the physicochemical properties of a potential drug without covalent chemical modification, thereby maintaining its efficacy. Drugs without ionisable functional groups can also be modified this way whereas salt formation, currently the most common modification to improve physicochemical properties inherently requires a drug to be ionisable[3].

Weak interactions such as hydrogen bonds, van der Waals forces and π-π interactions are the driving force behind co-crystal formation. Aakeroy *et al*.[4] initially introduced the concept of a supramolecular synthon in crystal systems referring to repeating units which form consistently when certain functional groups are present in the molecules. These synthons can be formed between like functional groups (homosynthons) or different groups (heterosynthons).

Various groups have conducted analyses of the Cambridge Structural Database (CSD) to examine the presence and prevalence of synthons in currently known crystal structures [5-7]. It has been found that synthons are present in many systems and comparative studies have found that in many cases synthon formation is dictated by Etter's rules of hydrogen bonding *i.e.* the strongest donor bonds to the strongest acceptor[8, 9]. The consistency with which these

groups bond has formed the basis of crystal engineering which aims to develop crystalline systems with novel properties by exploiting the formation of synthons. For obvious reasons, the ability to engineer specific systems will optimise the drug design and formulation process, allowing significant reductions in research costs and increasing the number of drugs which make it to market.

In 2011, Mukherjee *et al.*[10] reported three polymorphs of the 4,4′-bipyridine:4-hydroxybenzoic acid co-crystal. This co-crystal is particularly interesting as the effect of the different acidities of the hydroxyl and carboxylic acid hydrogens on preferred synthon formation can be examined. The polymorphs differed in the primary synthon present in each of the structures and have consequential effects on crystal packing and other properties. Thermal studies carried out by Mukherjee *et al.*[10] confirmed different melting points for each of the polymorphs and computational studies were used to speculate on the stabilities of the polymorphs. It was found that Form I was the more stable form. Here we present charge density studies of 4-hydroxybenzoic acid (4HBA) (**1**), 4,4′-bipyridine (44BP) (**2**) and one of the polymorphs (Form II) (**3**) and rationalise the physical features exhibited by the polymorph in terms of its electron density distribution (EDD).

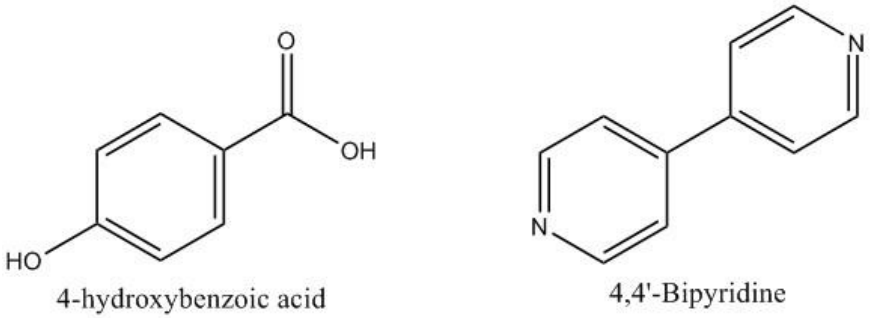

Figure 1: Chemical structure of 4-hydroxybenzoic acid (4HBA) (**1**) and 4,4′-bipyridine (44BP) (**2**).

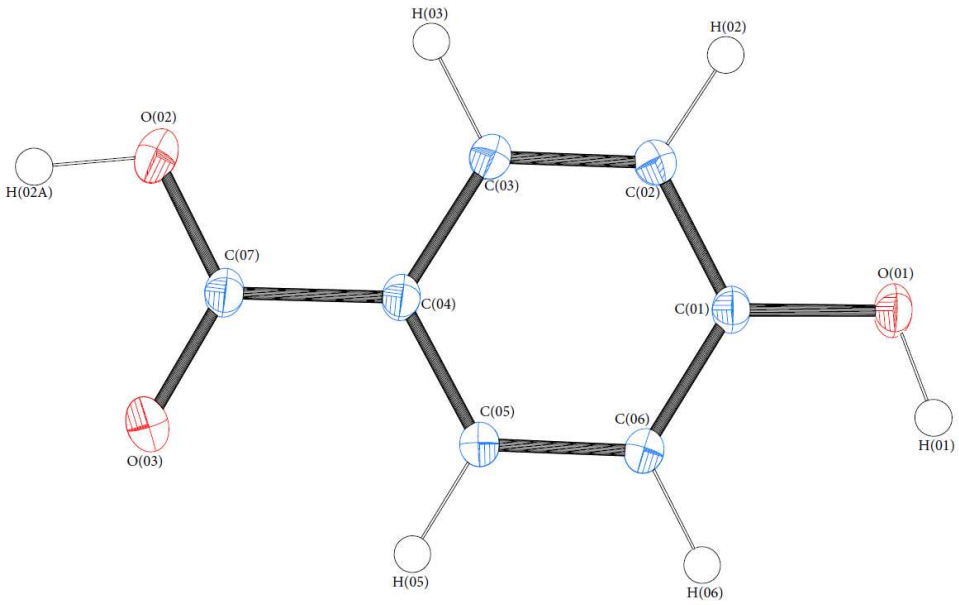

Figure 2: ORTEP diagram of 4HBA (**1**). Thermal ellipsoids are shown at the 50% probability level[11].

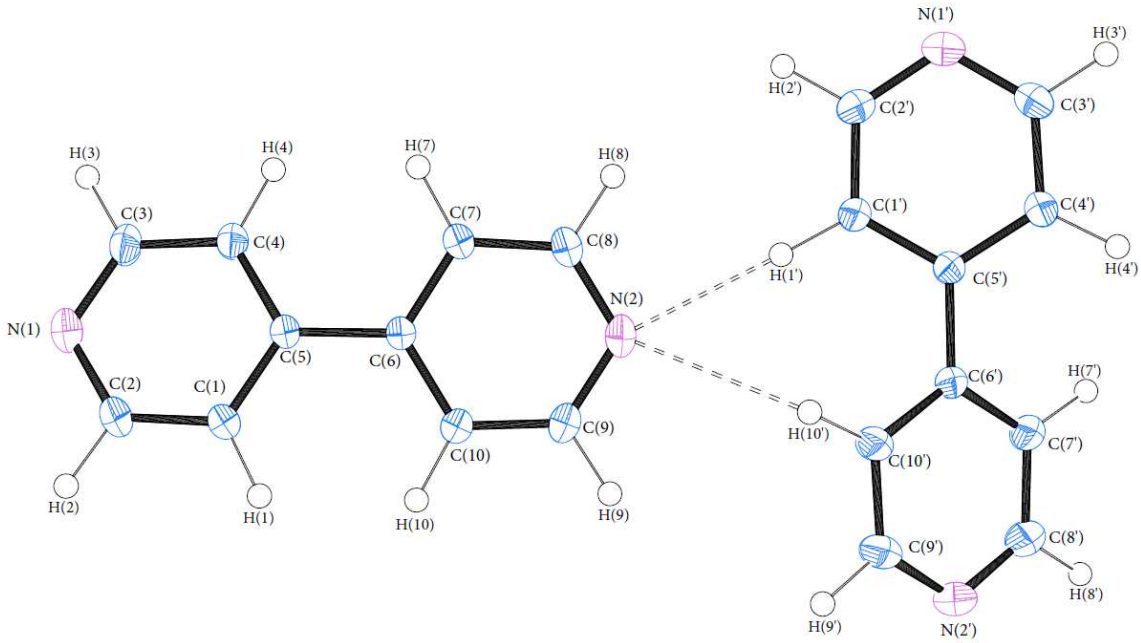

Figure 3: ORTEP diagram of 4,4′-bipyridine (**2**). Thermal ellipsoids are shown at the 50% probability level[11] .

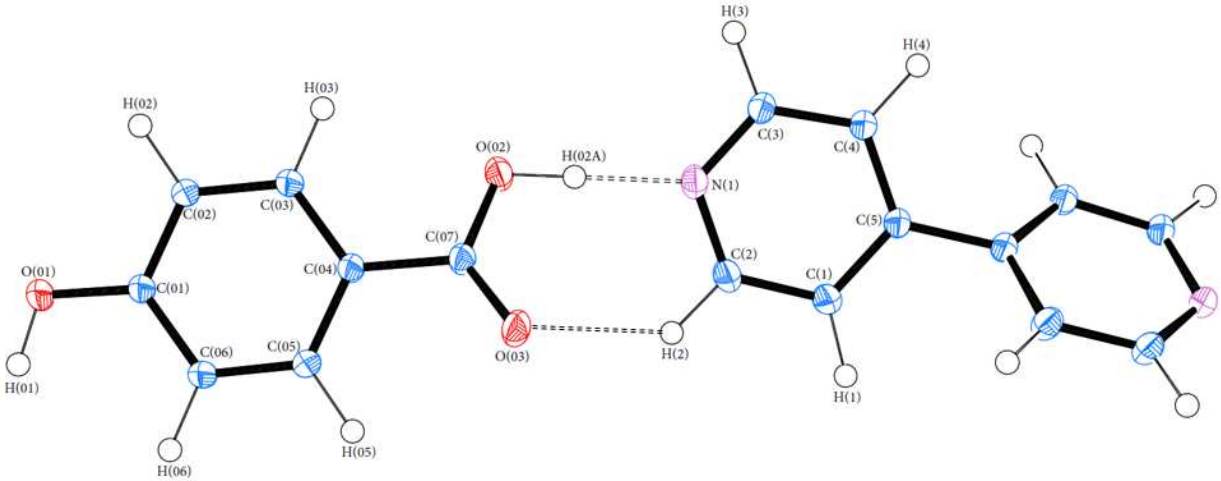

Figure 4: ORTEP diagram of the 4HBA-44BP co-crystal (**3**). Thermal ellipsoids are shown at the 50% probability level[11].

Methods

Raw materials (**1**) and (**2**) were purchased from Sigma Aldrich and used without further purification. Crystals of (**1**) were grown *via* slow evaporation from ethanol. Crystals of (**2**) were taken from materials purchased. Co-crystals of (**3**) were prepared following the method described by Mukherjee *et al.*[10]. Briefly, equimolar amounts of (**1**) and (**2**) were ground in a mortar and pestle until a fine powder was formed. The mixture was then dissolved in methanol and allowed to evaporate at room temperature.

Details on the collection, integration and reduction of data can be found in the supporting information. The multipole refinement procedure used has been reported in previous publications[12-14]. Refer to Table 1 for selected crystallographic information from the independent atom model (IAM) and multipole (*EXP*) refinements.

Table 1: Selected crystallographic information for (**1**), (**2**) and (**3**)

	1	2	3
Formula	$C_7H_6O_3$	$C_{20}H_{16}N_4$	$C_{17}H_{14}O_2N_3$
Molecular Mass	138.12	312.37	294.30
Crystal size (mm)	0.3 x 0.25 x 0.2	0.2 x 0.4 x 0.5	0.25 x 0.2 x 0.3
Temperature (K)	150	150	150
Crystal system	Monoclinic	Triclinic	Monoclinic
Space group	$P2_1/c$	$P\bar{1}$	$C2/c$
a (Å)	6.317(7)	8.693(2)	13.976(1)
b (Å)	5.200(1)	8.735(2)	11.628(3)
c (Å)	18.248(1)	10.982(2)	13.501(4))
α (°)		85.14(2)	
β (°)	92.11(2)	85.37(2)	114.19(4)
γ (°)		98.95(2)	
Volume (Å^3)	597.97(2)	813.80(3)	2001.41(1)
Z	4	2	4
Refinement Method	Full-matrix least-squares on F^2	Full-matrix least-squares on F^2	Full-matrix least-squares on F^2
No. of reflections collected	128328	55114	50126
No. unique	9616	13284	11414
R_{int}	0.037	0.0162	0.0161
Completeness (%)	98.3	99.1	99.3
No. reflections used	9636	19186	11448
ρ_c (g cm^{-1})	1.534	1.275	0.977
F(000)	288	328	616
μ (mm^{-1})	0.122	0.078	0.068
sin θ/λ_{max}	1.25	1.00	1.11
θ range for data collection (°)	3.233-62.673	2.920-45.294	3.244-52.157
Index ranges	$-15 \le h \le 15$ $-13 \le k \le 12$ $-45 \le l \le 45$	$-17 \le h \le 17$ $-17 \le k \le 17$ $-21 \le l \le 21$	$-31 \le h \le 30$ $-25 \le k \le 25$ $-29 \le l \le 29$
IAM Refinement			
Final $R1$, $wR2$	0.0381, 0.130	0.0470, 0.150	0.0356 0.114
Goodness of fit	1.021	1.018	1.070
Residual density (e Å^{-3})	-0.31, 0.57	-0.27, 0.49	-0.34, 0.54
Multipole Refinement			
N_{obs}/N_{var}	28.5	16.76	23.07
$R(F)$, $R(F^2)$, all data	0.0281, 0.0283	0.0271,0.0298	0.0214, 0.0299
$R_w(F)$, $R_w(F^2) > 2\sigma(F)$	0.0309, 0.0571	0.0290, 0.0551	0.0256, 0.0467
Goodness of fit	1.3891	1.4609	1.4047
Residual density (eÅ^{-3})	-0.161, 0.197	-0.126, 0.116	-0.111, 0.173

Results

Geometry

Bond lengths and angles for all experimental structures were obtained from the EXP refinement outputs. For each compound, the X-ray structure was in excellent agreement with results reported in the literature with mean differences in bond lengths of 0.029, 0.046 and 0.044 Å for (**1**), (**2**) and (**3**), respectively[15-17]. Similarly, the mean differences in angles were 0.050, 0.036 and 0.039°. Refer to Supplementary Tables S4-21 for a full list of bond lengths and angles for all structures. The crystal structure of (**1**) contained one molecule of 4HBA in the asymmetric unit. The asymmetric units of (**2**) and (**3**) both contained more than 1 molecule with (**2**) containing two 44BP molecules in a T-shaped arrangement and (**3**) containing one molecule of 4HBA and half a 44BP molecule with the remainder generated by symmetry (-*x*+1, *y*, -*z*+1.5) in an alternating pattern. Refer to Figures 2-4 for ORTEP diagrams and labelling schemes.

The hydroxyl and carboxylic acid groups on 4HBA exhibit some conformational flexibility and this is seen in the different conformations of 4HBA exhibited in (**1**) and (**3**). In (**1**), the torsion angle C(06)-C(01)-O(01)-H(01) describing the angle between the hydroxyl group and aromatic ring is -14.11° while the torsion angle between the carboxylic acid group and aromatic ring, C(03)-C(04)-C(07)-O(02) is 3.84°. The inverse is true in (**3**) where the conformations are virtually reversed with values of -2.27 and -19.68° respectively for the same torsion angles. The cause of the difference in the torsion angles in 4HBA between the single and co-crystals can be seen in the packing diagrams of (**1**) and (**3**) in Figure 5. Examination of the packing diagram of (**1**) shows a homosynthon between the carboxylic acid groups of 4HBA with the hydroxyl groups being involved in holding these dimers together. The hydroxyl group acts as both hydrogen bond donor and acceptor, and along with crystal packing effects may be the cause of the movement of the group away from a planar

position. A heterosynthon between the 4HBA carboxylic acid group and pyridine group in 44BP is the primary bonding motif in (**3**). The hydroxyl group is involved in a single hydrogen bond linking the other units together. The reduced strain on the hydroxyl group may account for a reduced rotation away from the plane of the aromatic ring. In both cases, the synthons formed agree with Etter's rules of hydrogen bonding[8, 9].

The 44BP molecule also undergoes a conformational change between (**2**) and (**3**). A previous study has found that the lowest energy state of a 44BP molecule is not when it is planar but when the torsion angle between the rings is 38.6°[18]. The two 44BP molecules have torsion angles of 16.62 and -34.54° respectively. In (**3**), the torsion angle of the 44BP molecule is -48.44°. None of these molecules are at the lowest energy state but weak interactions such as π-π interactions within the crystal help to stabilise the system. Figure 6 shows the variation in torsion angles in the 44BP molecules present in (**2**) and (**3**).

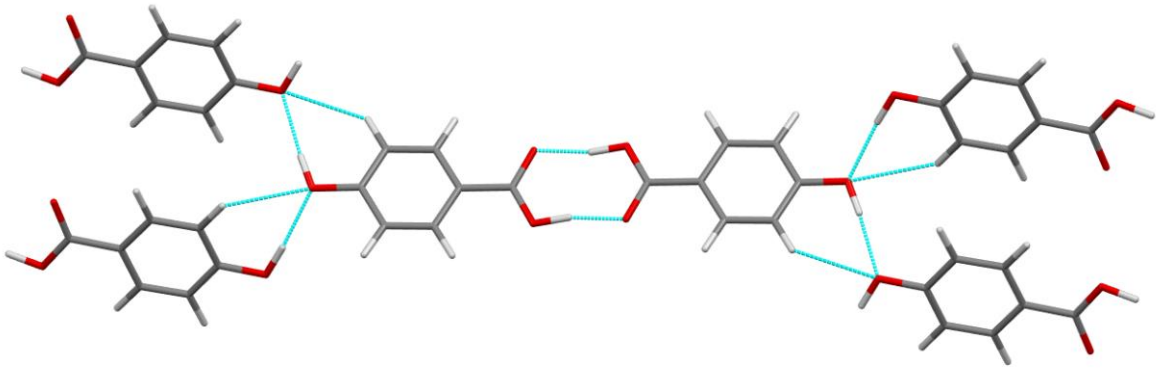

(a)

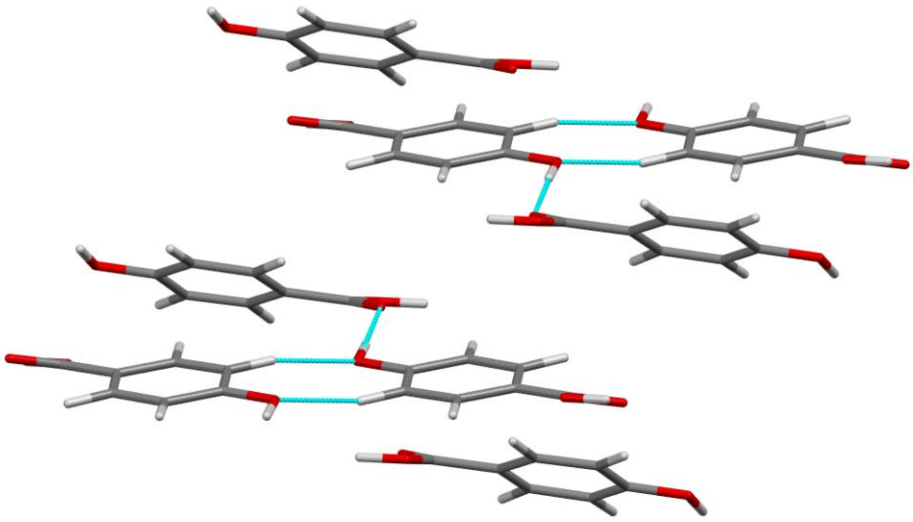

(b)

Figure 5: Packing diagrams of 4HBA in (a) (**1**) and (b) (**3**)[19]. 44BP molecules have been omitted for clarity. Refer to Figure S2 in the supplementary information for a full packing diagram.

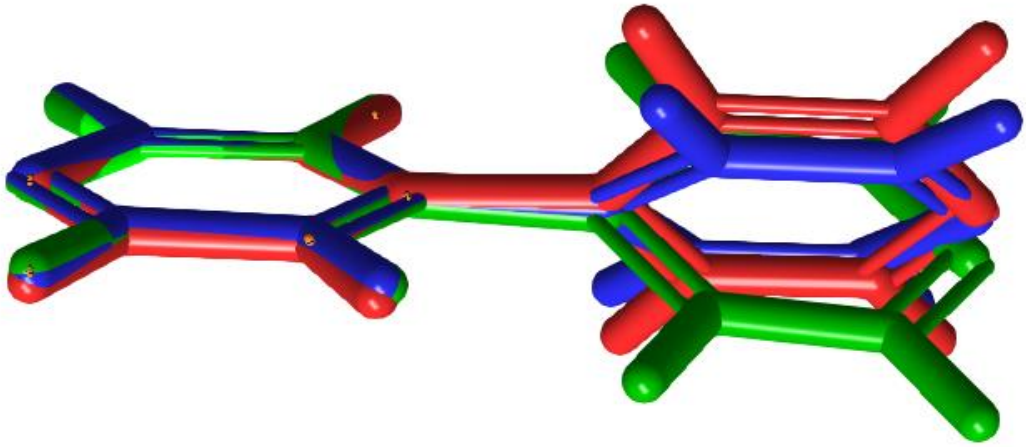

Figure 6: Structural overlays of 44BP in (**2**) (blue and green) and 44BP in (**3**) red[20].

Topological analysis

Topological analysis of both experimental and theoretical models using Bader's quantum theory of atoms in molecules (QTAIM)[21] was carried out and completeness of the analysis was verified through satisfaction of the Poincaré-Hopf, or its crystalline equivalent, the Morse relationship[22]. There was excellent agreement between the topological parameters of the EXP and SP models. The mean differences in ρ_{bcp} were found to be 0.124, 0.053 and 0.113 eÅ^{-3} for (**1**), (**2**) and (**3**) respectively. For $\nabla^2\rho_{bcp}$, mean differences of 4.60, 1.68 and 3.74 eÅ^{-5} were found. The largest discrepancies between the two models was found in the O-H bonds in the carboxylic acid (O(02)-H(02A)) and hydroxyl regions (O(01)-H(01)) of the 4HBA molecule in both (**1**) and (**3**). In (**1**), the differences were 41.94 and 25.77 eÅ^{-5} respectively while in (**3**) differences of 34.42 and 35.50 e Å^{-5} were noted. In both cases, the $\nabla^2\rho_{bcp}$ of the SP model was significantly more negative than the EXP. The involvement of these hydrogens in intermolecular hydrogen bonding in the EXP model and absence of crystal packing effects in the gas phase calculations is likely to account for the large discrepancy. Unsurprisingly, the O(02)-C(07) bond was also affected by the large discrepancies in the aforementioned bonds with mean differences of 25.02 and 17.63 eÅ^{-5} being recorded in (**1**) and (**3**) respectively. The EXP $\nabla^2\rho_{bcp}$ was significantly more negative compared to the SP model and is reflective of the shift in electron density towards O(02). Tables S22-27 in supplementary information show the full list of critical points found during topological analysis for all structures.

Hydrogen bonds

Hydrogen bonds can be classified into classical and non-classical hydrogen bonds bonds as defined by Koch *et al*.[23]. Classical hydrogen bonds are where both donor and acceptor are hetero atoms (N-H or O-H bonded to N or O) and non-classical bonds are, for

example, those of the form C-H···O and C-H···N. Both types of hydrogen bonds are characterised by relatively low ρ_{bcp} and a positive $\nabla^2\rho_{bcp}$ indicative of closed shell interactions. A total of 3, 8 and 5 hydrogen bonds were found for (**1**), (**2**) and (**3**) respectively. A comparison of all hydrogen bonds found that non-classical hydrogen bonds had longer acceptor to hydrogen and donor to acceptor lengths, compared to classical hydrogen bonds with all donor to acceptor distances greater than 3Å. These bonds also varied in linearity with the bond angle varying from 121.58 to 173.31° while the traditional hydrogen bonds were largely linear with the lowest angle being 167.84°.

Abramov [24] and Espinosa [25] developed a method using ρ_{bcp} and $\nabla^2\rho_{bcp}$ to calculate the kinetic (G), potential (V) and total (H) energy density in a bond and subsequently provide an estimation of its bond strength. The ratio -G/V can also be used to estimate the covalency of the bond, with a value between 0.5 and 1 indicating partly covalent character and a value greater than 1 being purely non-covalent [26]. H-bonds can be separated into three groups by their strengths; weak H-bonds (E_{HB} < 20 kJ mol^{-1}), moderate strength H-bonds (E_{HB} = 20-60 kJ mol^{-1}) and strong H-bonds (E_{HB} > 60 kJ mol^{-1})[27]. Details of the hydrogen bonds as determined by topological analysis are reported in Tables 2-3 for (**1**) and (**3**), respectively. Details for (**2**) can be found in Table S28 (ESI).

Table 2: Topological analysis of hydrogen bonding in (**1**). Standard uncertainties have been omitted from the Table for clarity. They are closely scattered around 0.02 eÅ^{-3} (ρ_{bcp}) and 0.05 eÅ^{-5} ($\nabla^2\rho_{bcp}$).

Bond	$\boldsymbol{\rho}$ (e Å^{-3})	$\boldsymbol{\nabla^2\rho}$ (e Å^{-5})	$\boldsymbol{\varepsilon}$	$\boldsymbol{D}_{H\cdots bcp}$ (Å)	$\boldsymbol{d}_{A\cdots bcp}$ (Å)	$\boldsymbol{G/E_h}$ (e Å^{-3})	$\boldsymbol{V/E_h}$ (e Å^{-3})	$\boldsymbol{H/E_h}$ (e Å^{-3})	$\boldsymbol{G/r}$	$\boldsymbol{E_{HB}}$ (kJ mol^{-1})
Intermolecular										
O(01)-H(01)···O(01)[a]	0.088	2.844	0.15	0.658	1.292	0.15	-0.09	0.05	1.67	36.71
C(06)-H(06)···O(01)[a]	0.042	0.562	1.85	1.252	1.509	0.03	-0.02	0.01	0.72	8.28
O(02)-H(02A)···O(03)[b]	0.389	2.561	0.01	0.511	1.11	0.29	-0.39	-0.11	0.74	152.94

Symmetry operators: [a] *-x*+2, *y*-0.5, *-z*+0.5; [b] *-x*, *-y*+1, *-z*+1

Table 3: Topological analysis of hydrogen bonding in (**3**). Standard uncertainties have been omitted from the Table for clarity. They are closely scattered around 0.02 eÅ^{-3} (ρ_{bcp}) and 0.05 eÅ^{-5} ($\nabla^2\rho_{bcp}$).

Bond	$\boldsymbol{\rho}$ (e Å^{-3})	$\boldsymbol{\nabla^2\rho}$ (e Å^{-5})	$\boldsymbol{\varepsilon}$	$\boldsymbol{D}_{H\cdots bcp}$ (Å)	$\boldsymbol{d}_{A\cdots bcp}$ (Å)	$\boldsymbol{G/E_h}$ (e Å^{-3})	$\boldsymbol{V/E_h}$ (e Å^{-3})	$\boldsymbol{H/E_h}$ (e Å^{-3})	$\boldsymbol{G/r}$	$\boldsymbol{E_{HB}}$ (kJ mol^{-1})
Intermolecular										
C(2)-H(2)···O(03)	0.086	1.109	0.08	1.028	1.391	0.07	-0.05	0.01	0.76	20.55
O(02)-H(02A)···N(1)	0.395	4.445	0.06	0.514	1.104	0.38	-0.45	-0.07	0.96	173.4
C(02)-H(02)···O(01)[a]	0.035	0.0965	0.67	0.933	1.493	0.05	-0.03	0.02	1.37	11.1
C(4)-H(4)···O(02)[b]	0.046	0.949	0.02	0.924	1.471	0.05	-0.03	0.02	1.07	12.31
O(01)-H(01)···O(03)[c]	0.223	4.889	0.02	0.581	1.129	0.29	-0.5	0.05	1.32	95.69

Symmetry operators: [a] *-x*+1.5, *-y*+0.5, *-z*; [b] *x*, *-y*, *z*+0.5; [c] *x*, *-y*+1, *z*-0.5

The hydrogen bonds found in (**1**) and (**3**) can be separated into two distinct groups; those involved in the formation of supramolecular synthons and those which bind the synthons together into repeating units forming the crystal lattice. Figure 5a clearly shows the carboxylic acid dimer homosynthon in (**1**) while the heterosynthon in (**3**) can be seen in Figure 7. These supramolecular synthons assemble in accordance with Etter's rules of hydrogen bonding, primarily that the strongest donor forms a bond with the strongest acceptor and the process is repeated until there are no more donors or acceptors[8, 9].

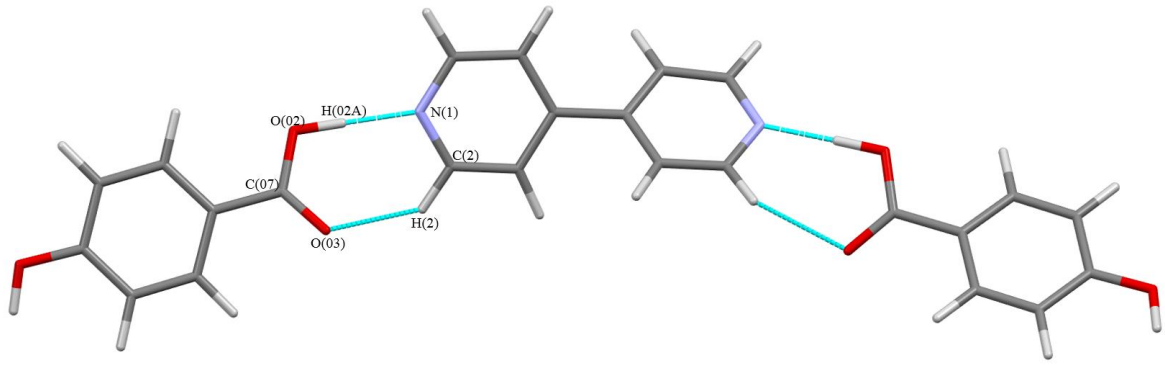

Figure 7: Diagram showing the heterosynthon in (**3**)[19].

Further analysis of the hydrogen bonds in (**1**) reveals the formation of the carboxylic acid dimer homosynthon is driven by the symmetrical O(02)-H(02A)···O(03) bond. Topological analysis reveals a strong bond with bond strength of 152.94 kJ mol^{-1} per bond, resulting in the homosynthon having a binding energy of 305.88 kJ mol^{-1}. Aside from the estimation of bond strength using the methods described above, other indicators are also present which predict the very strong nature of the bond. Figure 8 shows topological diagrams of the homosynthon and the interactions involving O(01) which bridge the 4HBA dimer units together. The lone pairs on all the oxygen atoms are clearly seen on the Laplacian diagrams (Figure 8a and 8c) as the areas of increased electron density (represented as more contour lines being packed more closely together) on the outer shell of the oxygen atoms as expected. The same notion is also represented in deformation density maps in Figures 8b and 8d. Here, the two oxygen lone pairs are represented as a pair of lobes with a relatively high electron density (once again represented *via* contour lines). The covalent nature of the C(07)-O(03) and C(07)-O(02) bonds can also be seen through the large density in the middle of the bond. Both Figures 8a and 8b show one of the lone pairs on O(03) is directly aligned with H(02A) contributing to the relatively large ρ value seen in Table 2. The large difference in polarity between O(03) and H(02A) is shown with the lone pair of O(03) clearly having a charge concentration (shown through the contour lines) while the hydrogen atom clearly

shows charge depletion. Furthermore, it is well known that the strength of a bond is inversely related to the bond length. In this case, the distance from the hydrogen and acceptor to the bond critical point ($d_{H\cdots bcp}$ and $d_{A\cdots bcp}$) is very small at 0.511 and 1.11 Å respectively. Examination of Figures 8c and 8d, which depict the bifurcation of O(01) show that the lone pairs of O(01), are directly aligned with H(01) and H(06), but the strength of these bonds is significantly weaker than that found in the homosynthon with estimated strengths of 8.28 and 36.71 kJ mol^{-1}. The $d_{H\cdots bcp}$ and $d_{A\cdots bcp}$ values are also larger in these cases with the weakest bonds having the largest distance of 1.252 and 1.509 Å, respectively. Thus, lone pair directionality does have a significant effect on bond strength, but $d_{H\cdots bcp}$ may play a more prominent role in predicting bond strength.

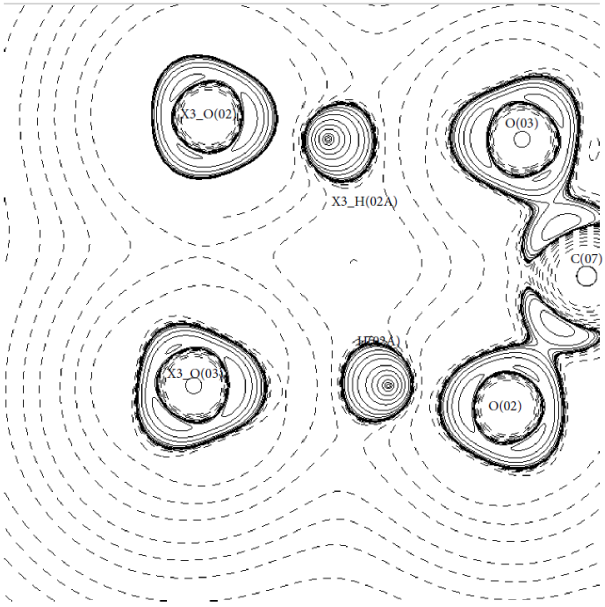

(a)

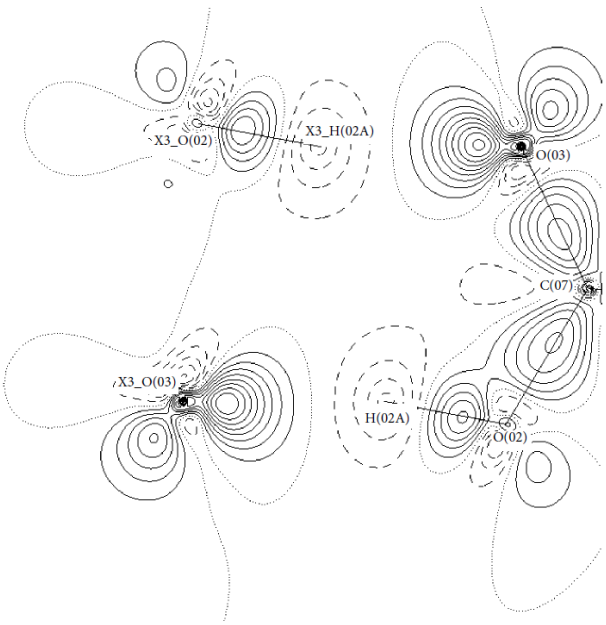

(b)

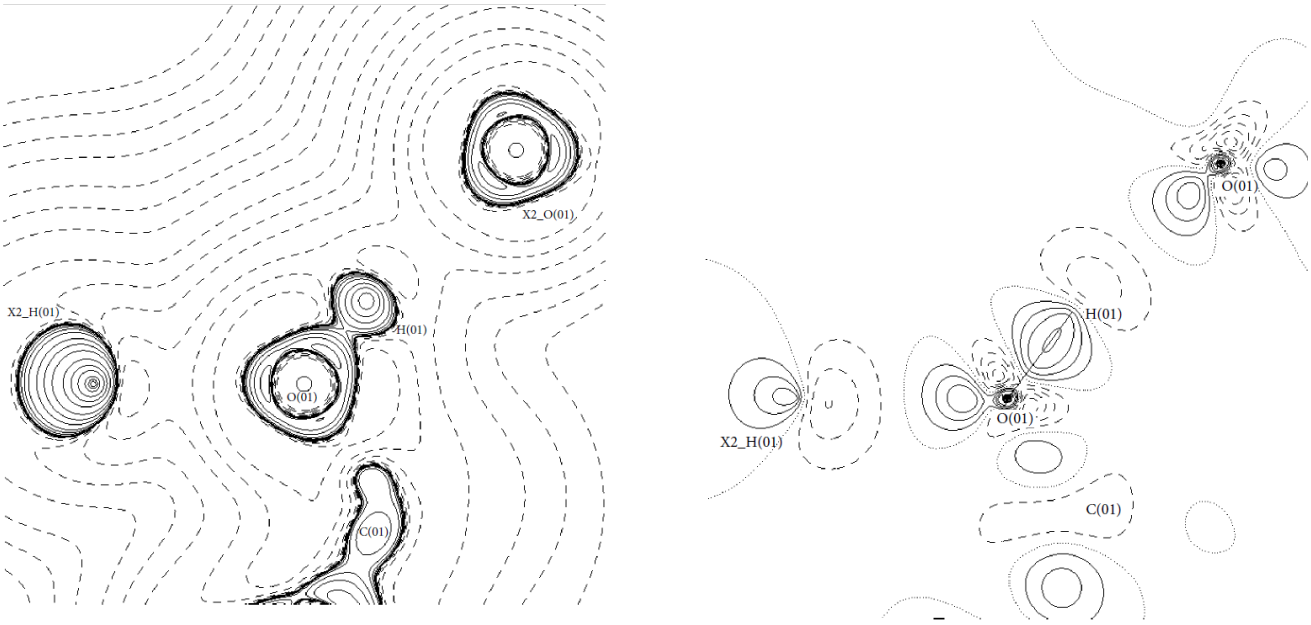

(c) (d)

Figure 8: $-\nabla^2\rho$ and deformation density maps for (a), (b) O(03)-C(07)-H(02A) plane in (**1**) and (c),(d) C(01)-O(01)-H(01) plane in (**1**). Solid lines in the Laplacian maps represent regions of charge concentration while dashed lines represent charge depleted regions. Similarly, for the deformation density maps, solid lines represent regions of positive electron density while dashed lines represent a negative electron density.

Similar findings can be seen in (**3**) with the formation of a heterosynthon between 4HBA and 44BP molecules rather than a carboxylic acid homosynthon. The C(2)-H(2)···O(03) and O(02)-H(02A)···N(1) bonds comprise the heterosynthon with bond strengths of 20.55 and 173.40 kJ mol^{-1}, respectively. Examination of topological diagrams of the heterosynthon in Figure 9 shows that the lone pairs of O(3) and N(1) are directly aligned with H(2) and H(02A), respectively, but there is a large difference in the hydrogen to critical point distance (0.514 *vs.* 1.028 Å) explaining the disparity in bond strength. The binding energy of this association (193.95 kJ mol^{-1}) is clearly less than the association energy of the homosynthon in (**1**). At first glance, the result may be contrary to what is expected where the most stable form will be present. An examination of the intermolecular hydrogen bonds in (**3**) shows one of the bonds (O(01)-H(01)···O(03)) has a bond strength of 95.69 kJ mol^{-1}. The

atom O(03) is also involved in this interaction and its bifurcation (as can be seen in Figure 9) results in a spread of its electron density over two areas resulting in the formation of two strong interactions; one involved in synthon formation and the other as a stabilising force with a combined energy of 270 kJ mol $^{-1}$. This result highlights the effect of introducing an extra component (co-former) into crystalline systems to form co-crystals; the co-former allows the initial molecule to exist in an otherwise thermodynamically unstable state potentially resulting in a modified energy surface which may manifest as different physical properties.

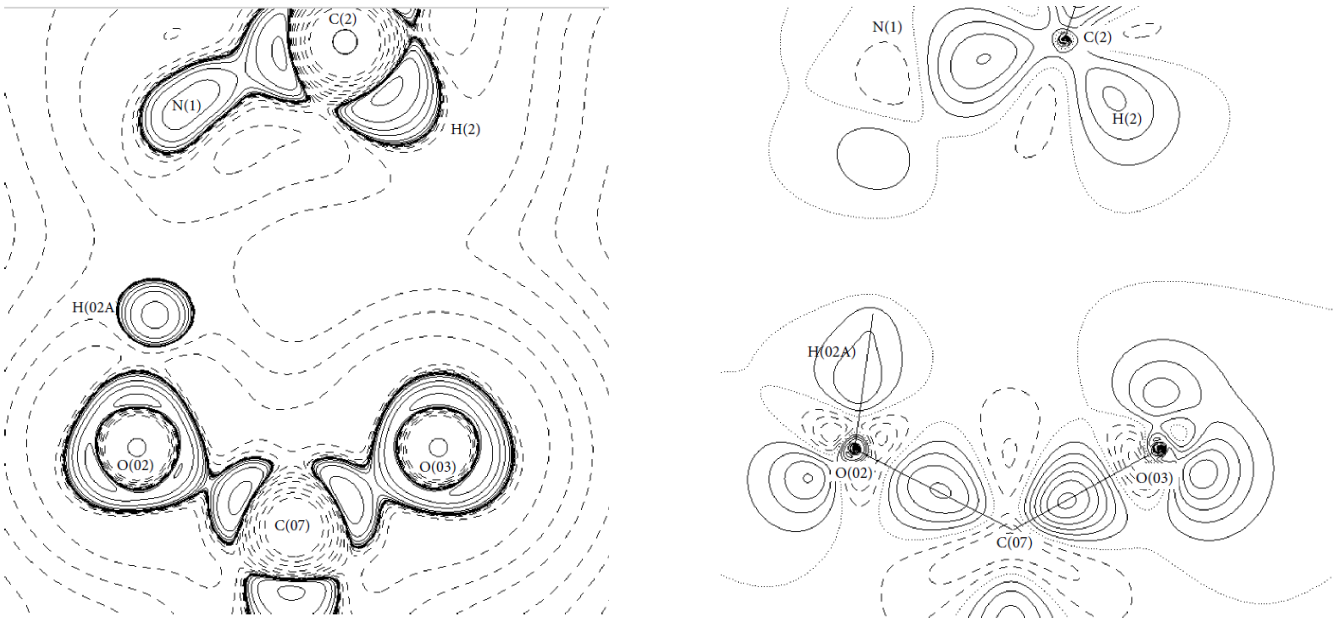

(a) (b)

Figure 9: $-\nabla^2\rho$ and deformation density maps for the O(03)-O(02)-N(1) plane in (**3**). Solid lines in the Laplacian maps represent regions of charge concentration while dashed lines represent charge depleted regions. Similarly, for the deformation density maps, solid lines represent regions of positive electron density while dashed lines represent a negative electron density.

The role played by the $d_{H\cdots bcp}$ and $d_{A\cdots bcp}$ distances in predicting bond strength can also be seen in a comparison of the strength of hydrogen bonds which involve nitrogen in (**2**)

and (**3**) in similar patterns. In (**2**), N(2) is involved in two bond with H(1') and H(10') with respective strength of 8.36 and 18.8 kJ mol^{-1} while the single bond formed by N(1) in (**3**) is significantly stronger at 173.4 kJ mol^{-1}. This disparity is especially striking as there is a whole order of magnitude difference between the strength of the bonds. As mentioned above, the $d_{H\cdots bcp}$ distance is approximately 0.5 Å in (**3**) while the distances in (**2**) are significantly longer (~1.2 and 0.8 Å for H(1') and H(10'), respectively).

Hirshfeld surfaces

Three dimensional Hirshfeld surfaces and corresponding two dimensional fingerprint plots were generated using the CrystalExplorer[28] program. Hirshfeld surfaces provide a visual representation of the effect a molecule's electron density has on the space around it in a crystalline system. The Hirshfeld surfaces are shown in Figures 10 and 11 for (**1**) and (**3**). Figure S5 (ESI) shows the Hirshfeld surfaces for (**2**). Areas where intermolecular interactions are present are highlighted red in the diagrams. In accordance with previous findings, red spots are located near the oxygen and nitrogen atoms in the 4HBA and 44BP molecules respectively and their associated hydrogen atoms. Figures 12 and 13 show 2 dimensional fingerprint plots for the complete molecules and specific interactions for (**1**) and (**3**). Similar plots for (**2**) are located in Figure S6 (ESI). d_i refers to the distance from the Hirshfeld surface to the nearest nucleus inside the surface while d_e refers to the same distance to the nearest nucleus external to the surface. Analysis of the fingerprint plots for (**1**) show that O···H bonds contribute most towards the Hirshfield surface accounting for 33.9% of all interactions. This is unsurprising as O···H bonds connect the dimers to each other and play a role in linking the dimers together. C···H and H···H interactions are the remaining significant interactions and this may be attributed to van der Waals forces present in the system. Unsurprisingly, N···H interactions dominate in (**2**) accounting for 20.7% of interactions. A similar situation to (**1**) is seen in (**3**) with the O···H interactions accounting for 20.9% of all

interactions. N···H bonds are primarily involved in the heterosynthon and as mentioned above the bond is considered weak. Unsurprisingly, N···H bonds only account for 4.8% of interactions. Interestingly, H···H and C···H bonds account approximately 60% of weak interactions in (**3**). This is attributed to the van der Waals forces in the system. These forces are separate from π-π stacking interactions which only account for 7.4% of interactions. These are present in (**3**) but not in (**1**) due to the introduction of the 44BP molecule.

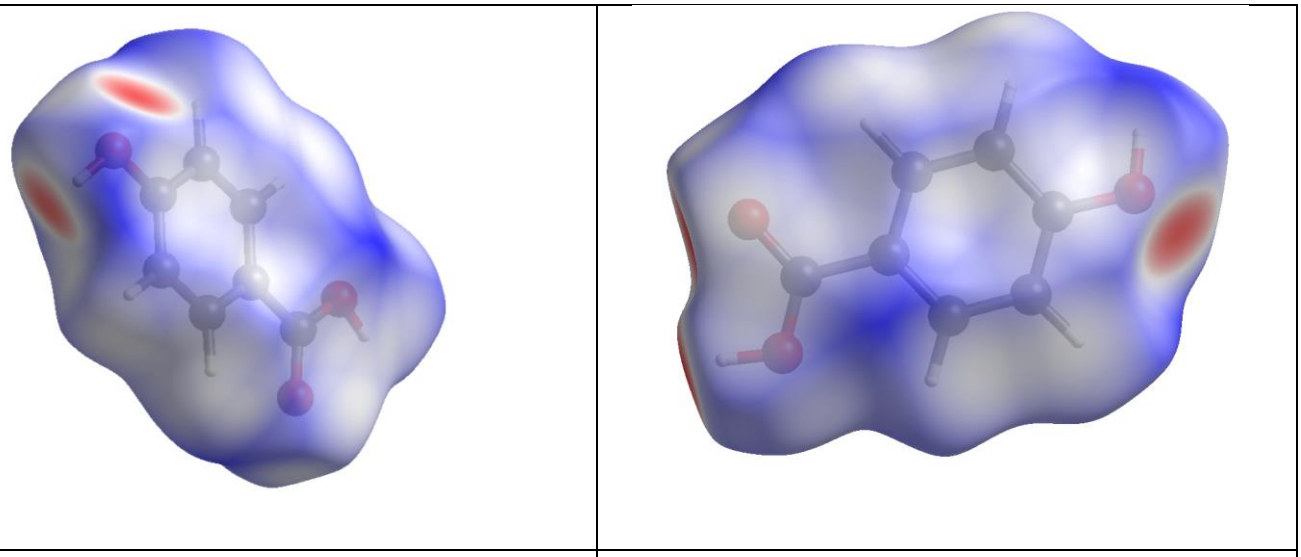

(a) (b)

Figure 10: Hirshfield surfaces for (**1**)[29].

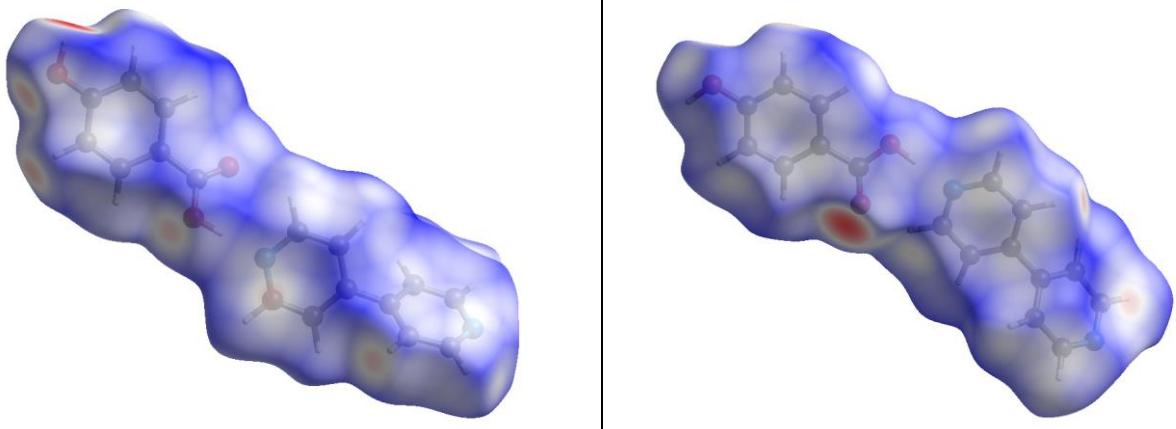

(a) (b)

Figure 11: Hirshfield surfaces for (**3**)[29].

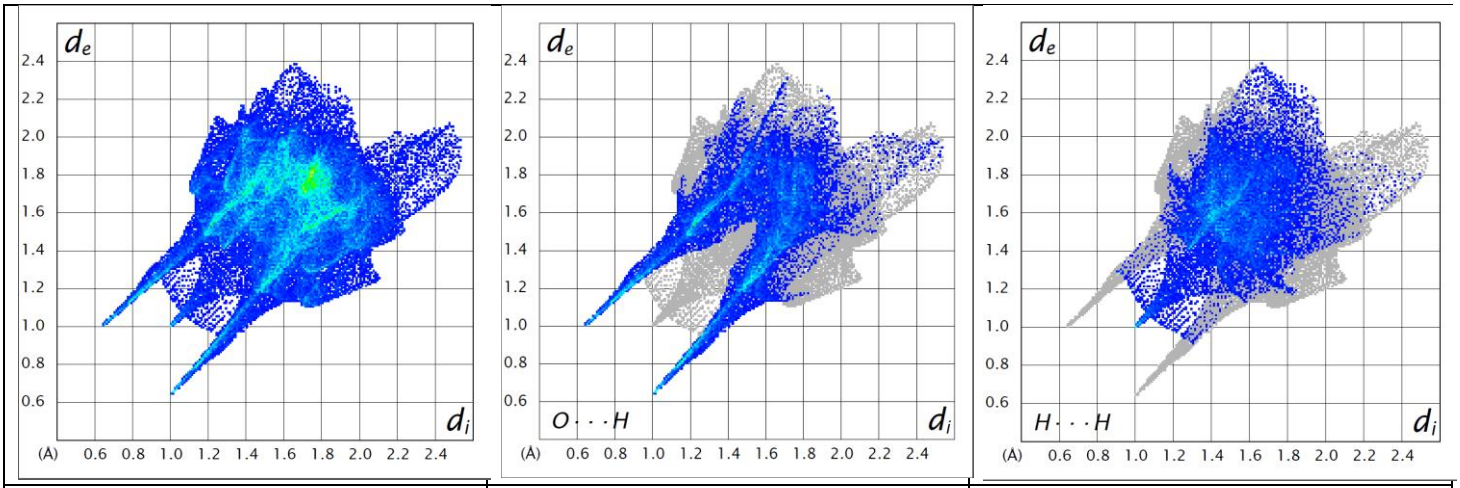

(a) (b) (c)

Figure 12: 2-Dimensional fingerprint plots of (a) all interactions in (**1**), (b)O···H interactions in (**1**) and (c) H···H interactions in (**1**) [29].

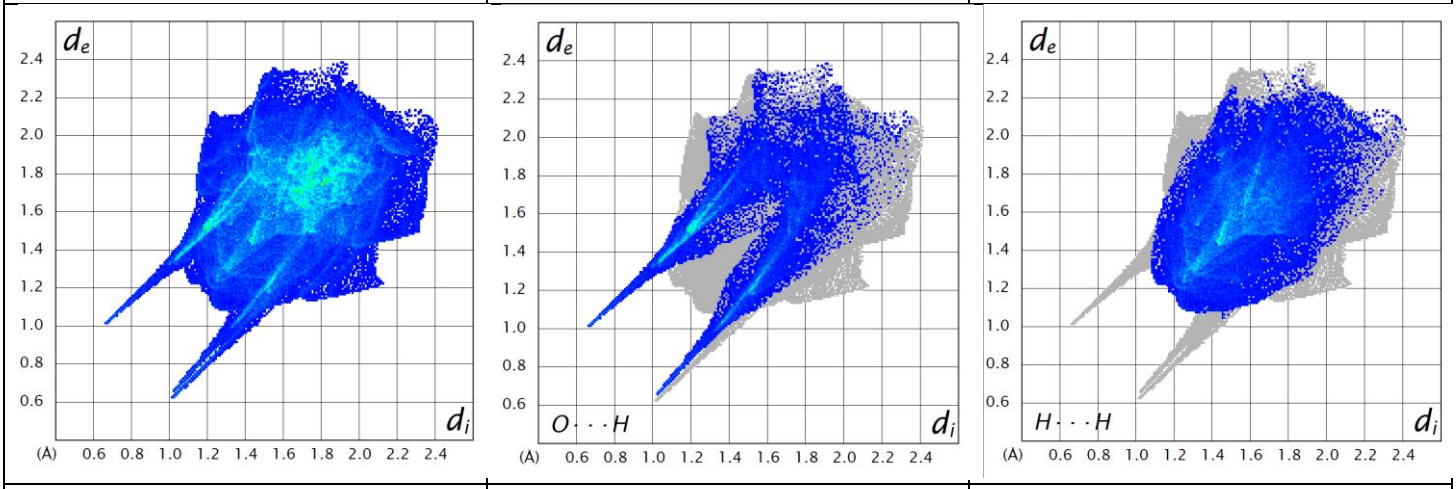

(a) (b) (c)

Figure 13: 2-Dimensional fingerprint plots of (a) all interactions in (**3**), (b) O···H interactions in (**3**) and (c) H···H interactions in (**3**)[29].

Atom charges

Integrated atomic basin charges were also determined from topological analysis of (**1**), (**2**) and (**3**). There was excellent agreement between the charges obtained from the EXP

and SP models. The largest difference between the models was found in (**1**) and (**2**) in the O-H groups and nitrogen atoms respectively. In (**1**), O(02), O(03) and H(01) differed the most by approximately 0.1 e with the EXP model being more electron rich. A similar trend was seen with all four nitrogen atoms in (**2**) with the charge consistently overestimated in the EXP model by 0.3 e. These differences are due to the gas phase nature of the SP calculations compared to the EXP model thus not accounting for the intermolecular bonding and crystal packing which occurs in a crystalline lattice. This is especially relevant in the case of the 44BP molecule as it is well known the conformation is heavily influenced by its supramolecular environment [30, 31]. Further analysis of the atom charges between atoms in (**1**) and (**2**) and their analogous atoms in (**3**) found large differences in atoms, most of which were involved in heterosynthon formation – C(07), O(02), H(02A), N(1), H(2). The largest difference found was for H(02) (0.67 e) and can be attributed to its participation in hydrogen bonding with an intermolecular O(01) and various other weak interactions which were not present in (**1**). Differences of 0.43 and 0.23 e were seen for H(02A) and H(2) respectively. This is in accordance with the findings in the hydrogen bond section where the interaction is not as strong as the carboxylic acid homosynthon but still occurs due to the nitrogen being a better acceptor than the carbonyl oxygen. Changes in the atom charge of C(1) by 0.12 e may be due to an inductive effect of the local bonding environment. A complete list of atom charges can be found in Tables S32-34 (ESI).

Electrostatic potential

The molecular electrostatic potential (MEP) has an integral role in explaining the effect of the EDD gained from charge density analysis on physical outcomes in the system such as atom reactivities and the weak interactions which form. MEP maps are shown in Figures 14-16 and comparing these maps provides insights into the physical changes which

occur when co-crystallisation occurs as opposed to the formation of a single crystal. The MEP maps have been mapped onto an isosurface of ρ and have been plotted on the same scale for comparability. In accordance to previous findings mentioned above, the carboxylic acid and hydroxyl groups on the 4HBA molecule are significantly involved in hydrogen bonding in both (**1**) and (**3**). This can be seen in Figures 14-16 where those groups in (**1**) and (**3**) are surrounded by red and purple indicating highly electronegative regions. The relatively small size of the 4HBA molecule results in the aromatic region having slightly more electron localisation in the π system around the aromatic ring due to it being enclosed by electronegative groups. Unsurprisingly, there is a very even spread of charge in (**2**) indicating an even spread of electrons over the molecules. This is due to the π systems in the aromatic rings with some charge localisation on the nitrogen atoms due to them being slightly more electronegative. Visual analysis of (**3**) shows properties of the MEP present in both (**1**) and (**2**) with the heterosynthon region having high levels of complementarity between electronegative and electropositive regions and the aromatic systems showing even delocalisation of electrons. It can be said that the charge distribution across all three systems is relatively even with compounds (**1**) and (**3**) being electrostatically symmetrical and (**2**) being largely comprised of aromatic systems. This can be seen through the molecular dipole moments (MDM) of the system of 0.81, 3.18 and 1.70 D, respectively. The values here can be misleading as the large number of hydrogen bond donors and acceptors present especially in (**3**) provide sufficient charge differentials to promote further hydrogen bonding with water among other examples. These properties can only be derived experimentally from high resolution diffraction experiments and allow for further insights to be gained on the exact changes in electrostatics which occur in crystalline systems and upon co-crystallisation.

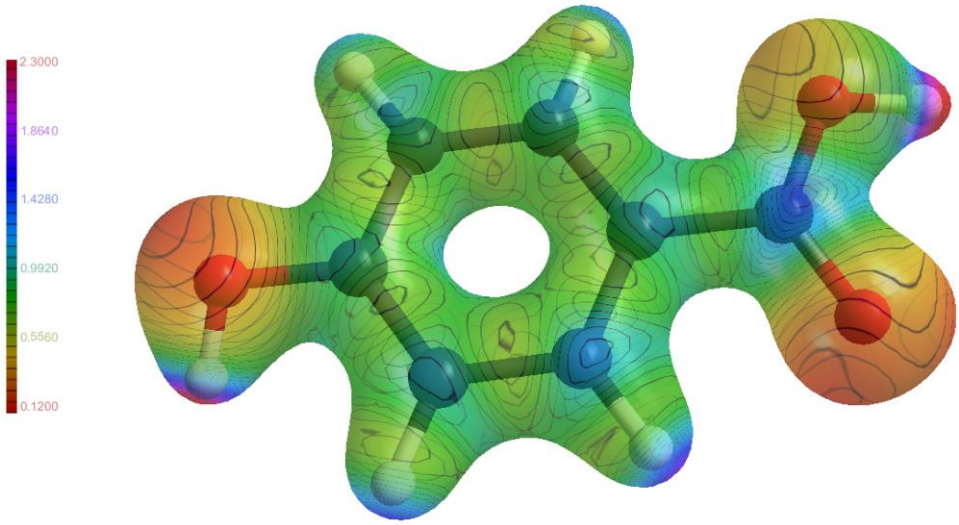

Figure 14: Molecular electrostatic potential maps of (**1**) mapped on an isosurface of ρ^{32}. The colour gradient has units of e per bohr.

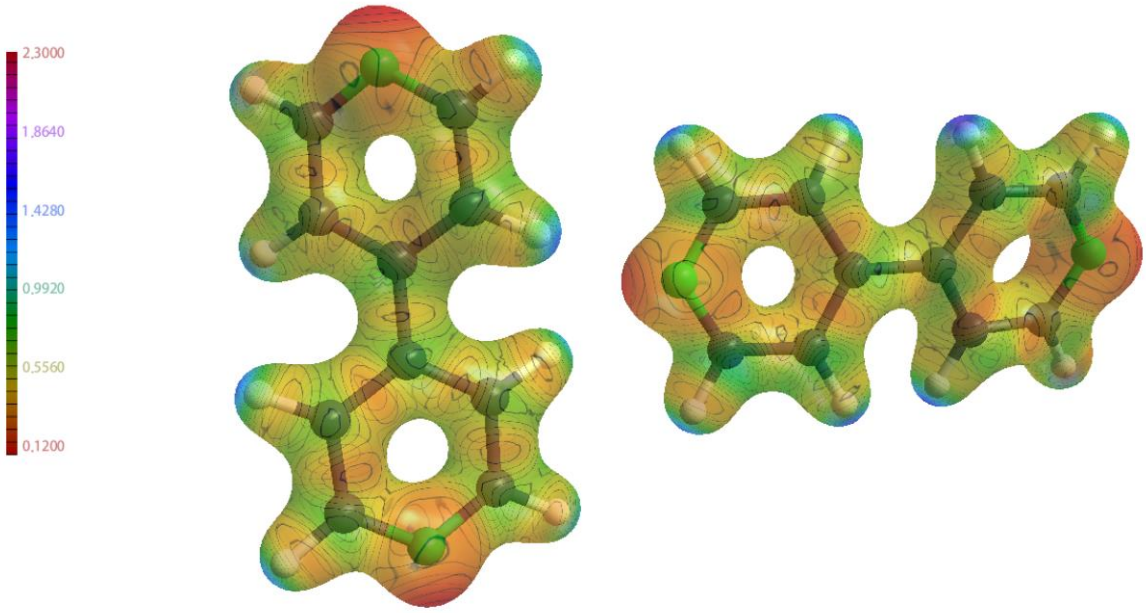

Figure 15: Molecular electrostatic potential maps of (**2**) mapped on an isosurface of ρ^{32}. The colour gradient has units of e per bohr.

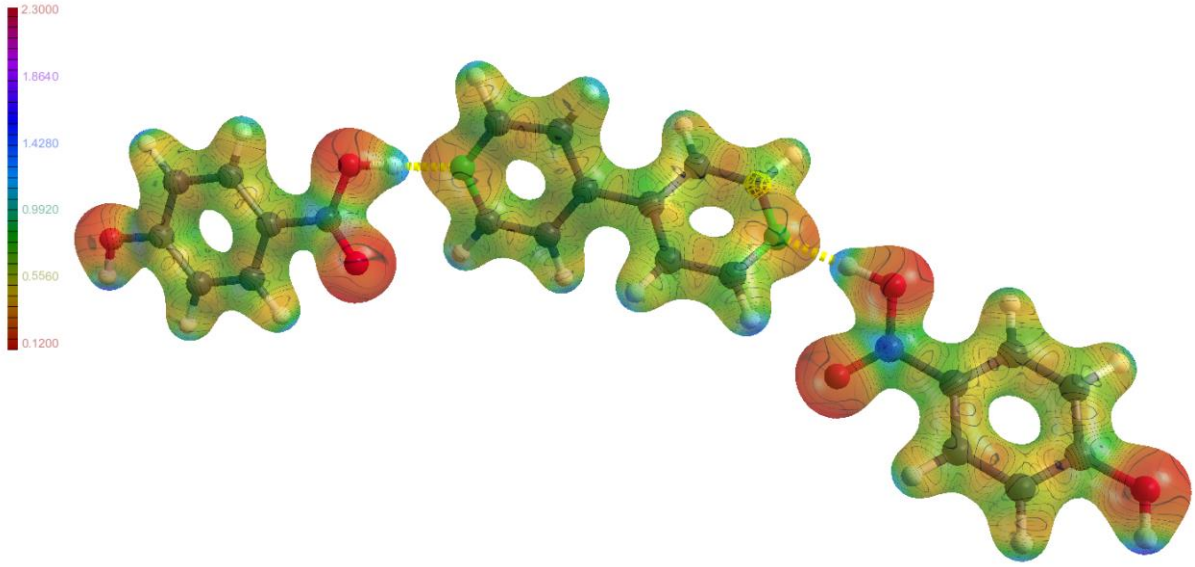

Figure 16: Molecular electrostatic potential maps of (**3**) mapped on an isosurface of ρ[32]. The colour gradient has units of e per bohr.

Lattice energies

The lattice energies of (**1**), (**2**) and (**3**) were determined for the EXP model to assess the effect of changes in charge distribution during the co-crystallisation process as described above on the overall stability of the system. This has physical implications such as the solubility of the co-crystal complex in solution compared to its individual counterparts. Two methods were used to calculate the lattice energy; the LATEN option in XD2006[33] and the PIXEL method developed by Gavezzotti[34], which partitions the electron density into 'pixels' which are then used for the calculation. The lattice energy from LATEN is considered to be the sum of the electrostatic interaction, repulsive, dispersive and penetrating electrostatic contributions as originally introduced by Spackman[35]. The exact potential multipole model (EPMM) method introduce and validated by Volkov et al.[36-38] as an alternative to the more computationally expensive exact potential (EP) method was used in XD2006. The electrostatic interaction term is a Buckingham type expansion in the form of a Taylor series[36], the repulsive and dispersive terms are fitted as single exponential functions where the

coefficients are read from tables previously published by Spackman[39] and the penetrating coulombic term is defined as the interaction of the spherical charge distribution of atom A with the deformation density distribution of atom B[35]. The PIXEL method takes a similar approach with the total intermolecular interaction energy defined as the sum of the coulombic, polarisation, dispersion and repulsion forces. Details of the equations used can be found in the appendix of Gavezzotti[40].

Table 4 shows the lattice energies calculated for all structures using both methods. Due to the asymmetric unit of (**3**) only containing half a 44BP molecule, the value of PIXEL was calculated as twice the lattice energy of a system containing a single 4HBA and 44BP molecule minus the lattice energy of a 44BP molecule alone in the same cell. The LATEN method consistently reported more negative values compared to the PIXEL method. Small difference in energy of ~20 and 10kJ mol^{-1} was reported for (**1**) and (**3**) while a larger differences ~200 kJ mol^{-1} were reported for (**2**). Spackman[41] previously discussed this discrepancy and attributed it to certain intermolecular bcp's not being found even though the Morse equation has been satisfied potentially due to the extremely flat nature of the electron density at these critical points; this is particularly relevant as critical points of hydrogen bonds often have very low electron density.

Table 4: Table of lattice energies for (**1**), (**2**) and (**3**) predicted by the LATEN[33] option in the XD package and the PIXEL[34] method.

Crystal	LATEN (kJ mol^{-1})	PIXEL (kJ mol^{-1})
(**1**)	-181.1	-162.5
(**2**)	-311.2	-110.5
(**3**)	-138.1	-149.0

The LATEN method indicated (**2**) to be the most stable followed by (**3**), then (**1**). The PIXEL method reported (**2**) to be the least stable with (**1**) found to be the most stable. Tables 5 and 6 show contributions of electrostatic, dispersion and repulsions force to the lattice energies calculated by the LATEN and PIXEL methods respectively.

Electrostatic forces are shown to account for twice as much of the lattice energy as dispersion forces in (**1**) in both methods This is also seen in Figure 17 which shows the energy frameworks diagrams for (**1**). The electrostatic forces are seen to be located near the homosynthon and are much more prominent compared to the dispersion forces. The LATEN and PIXEL methods differed in their breakdown of the lattice energy of (**2**) with the former reporting a larger contribution by dispersion forces (-261.3 kJ mol^{-1}) compared to electrostatic forces (-180.6 kJ mol^{-1}). These differences may be attributed to the differing treatment of polar hydrogen atoms in a system. The LATEN method allows input of hydrogen - acceptor distance and marking of highly polar hydrogens, which are then allocated different potentials for the calculations while the PIXEL method treats all hydrogens in the same way. This may introduce an inadvertent weighting scheme which affects the contributions of the different forces to the lattice energies. Figure S7 (ESI) shows the energy framework diagrams for (**2**) and it can be seen that the electrostatic forces are in the layers of 44BP while the dispersion forces are located between layers in the form of π-stacking. These aromatic interactions also account for the C···C and C···H interactions found in the fingerprint plots in Figure S6 (ESI). Both methods also report a large repulsive force (130.7 and 81.7 kJ mol^{-1} for the LATEN and PIXEL methods respectively) and can be attributed to unfavourable interactions of the π-systems.

In (**3**), the LATEN method found dispersion forces to be twice as large as electrostatic forces (-204.8 *vs*. -108.2 kJ mol^{-1}) while the inverse was reported by the PIXEL method (-

68.3 *vs.* -73.8 kJmol^{-1}). This could be due to the higher electron density associated with the stronger hydrogen bonds as discussed above with the PIXEL method potentially overestimating the contribution of these bonds to the overall lattice energy. The treatment of polar hydrogen atoms by the LATEN method may also be a factor. Figure 18 shows coulombic interactions to be more prominent compared to the dispersive forces, similar to findings using PIXEL. Once again, differences can be attributed to differences in methodology. Both PIXEL and CrystalExplorer use gas phase calculations *via* Gaussian[42] and TONTO[43] respectively and this may account for the similar results. Figure 18 shows the location of the different forces with coulombic forces dominating the heterosynthon (Figure 18a) and dispersion forces holding the layers together (Figure 18b) highlighting the conclusion that the co-crystal is held together by features from both (**1**) and (**2**). These differing results illustrates the need to compare different methods of calculating the same property as small differences during the procedure may lead to large changes in the results as seen here.

Table 5: Breakdown of the lattice energy obtained from LATEN[33] calculations into their individual components. Energies are given in kJ mol^{-1}.

Crystal	Electrostatic	Dispersion	Exchange-repulsion
(**1**)	-234.8	-169.1	222.8
(**2**)	-180.6	-261.3	130.7
(**3**)	-108.2	-204.8	174.8

Table 6: Breakdown of the lattice energy obtained from PIXEL calculations into their individual components. Energies are given in kJ mol^{-1}.

Crystal	Coulombic	Polarisation	Dispersion	Repulsion
(**1**)	-146.7	-75.1	-100.1	159.4
(**2**)	-58.8	-26.1	-107.6	81.7
(**3**)	-73.8	-50.3	-68.3	110.1

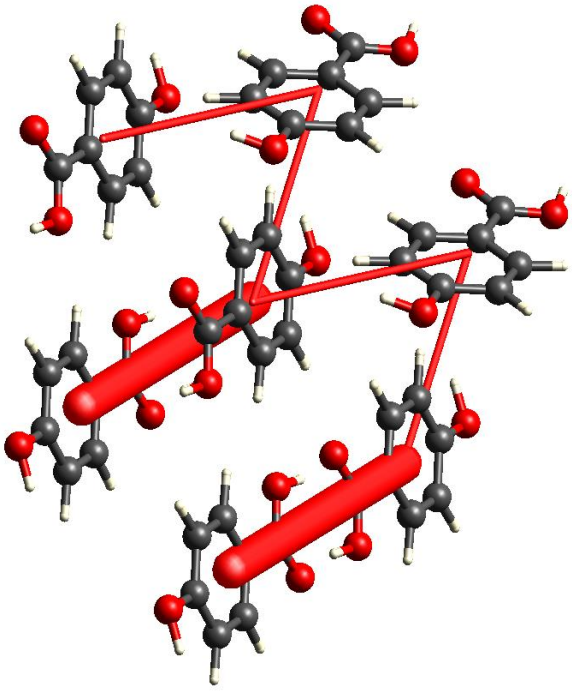

(a)

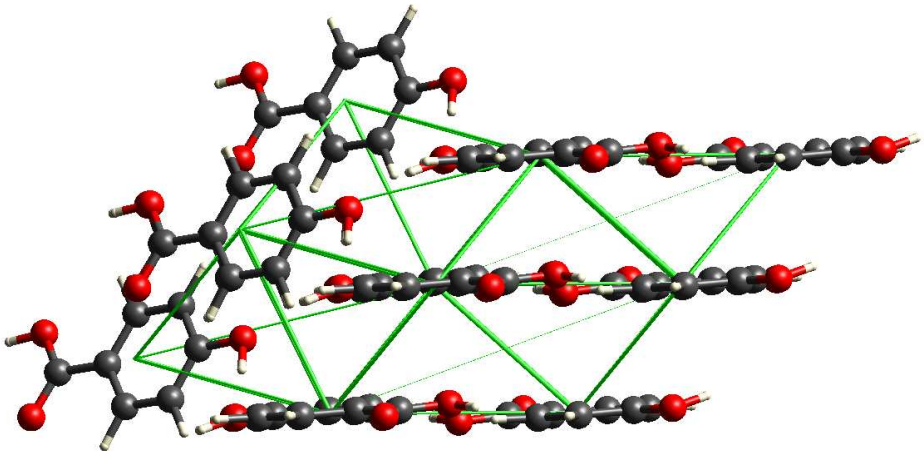

(b)

Figure 17: Energy frameworks for (**1**). The energy scale is 30 and energy threshold is zero. (a) coulombic forces (b) dispersion forces[29].

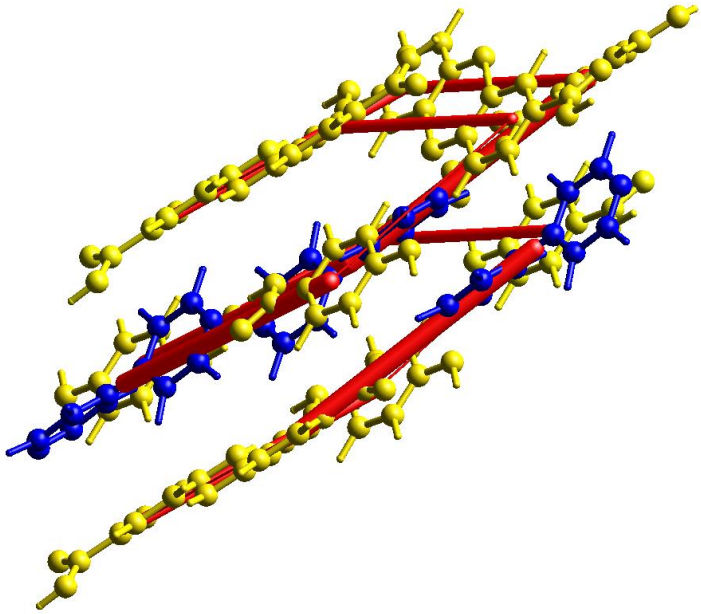

(a)

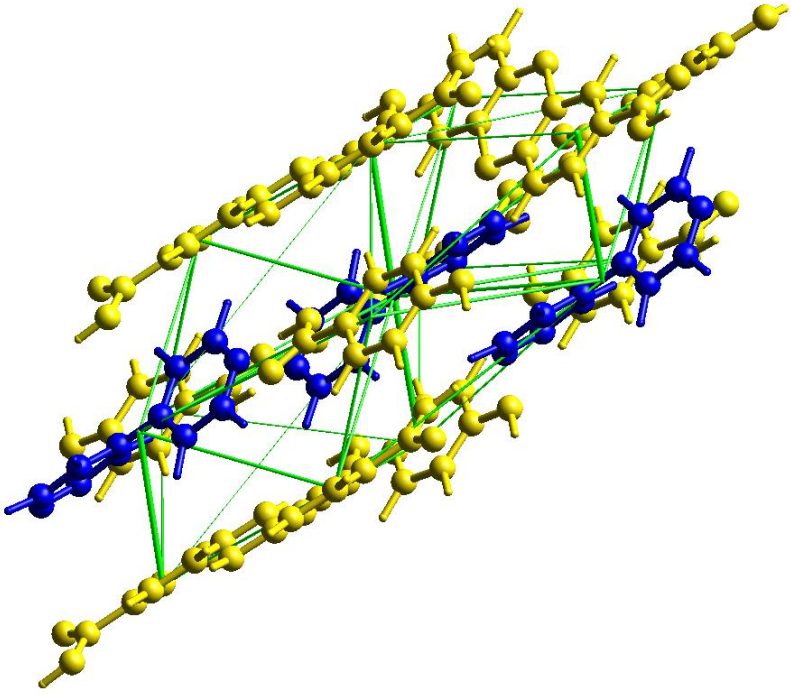

(b)

Figure 18: Energy frameworks for (**3**). The energy scale is 30 and energy threshold is zero. 4HBA molecules are colour coded yellow and 44BP molecules are blue; (a) coulombic forces, (b) dispersion forces[29].

Conclusion

Here we present an experimental EDD study of 4HBA (**1**), 44BP (**2**) and one polymorphic form of the 4HBA-44BP (**3**) co-crystal as reported by Mukherjee *et al.* [10] with the aim to rationalise the physical properties described by the authors *via* the electron density distribution. The asymmetric unit of (**1**) was found to contain a single 4HBA molecule, (**2**) contained two 44BP molecules in a T-shaped arrangement and (**3**) contained 4HBA and 44BP in a 2:1 ratio. Co-crystal formation is driven by a heterosynthon between a 4HBA and a 44BP molecule, while a carboxylic acid homosynthon is present between 4HBA molecules in (**1**). The binding energy of the homosynthon was found to be higher than that of the heterosynthon (305.88 *vs*. 193.95 kJ mol^{-1}), a finding that correlates with the lattice energy values. The relationship between the strength of weak interactions and the $d_{H\cdots bcp}$ and $d_{A\cdots bcp}$ values was also investigated and an inverse relationship was found in accordance with previous findings. This parameter was found to play a more prominent role in determining bond strength than lone pair directionality as seen through $-\nabla^2\rho$, however these two indicators should be used concomitantly to optimise bond strength predictions. Two-dimensional fingerprint plots reveal O···H and N···H interactions account for a large amount of weak interactions found. Lattice energy calculations were also carried out using the LATEN[33] and PIXEL[34] methods with both reporting (**1**) to be more stable than (**3**) by ~40 and 10 kJ mol^{-1} respectively. The agreement of relative stability between (**1**) and (**3**) across both methods is encouraging for future studies. These differences were discussed and attributed to small

differences in methodology. Although the crystalline structure of (**1**) was found to be more thermodynamically stable, a small reduction in stability with the addition of a co-former made possible due to a wider range of weaker interactions being formed highlight the potential of co-crystals and heterosynthons as a stepping stone for improving the physicochemical properties of pharmaceuticals. Additionally, these findings highlight the importance of using a variety of methods to calculate a single parameter as no method is infallible. Analysis of energy framework diagrams obtained from CrystalExplorer reveal coulombic forces dominate interactions in (**1**) and both coulombic and dispersion forces are prominent in (**2**) and (**3**) contains an even mixture of the two forces. In addition to comparing the changes that occur within a molecule when co-crystallisation occurs at an electronic level, this study also examined a homosynthon and heterosynthon in detail. The findings above indicate that heterosynthons allow more numerous weak interactions to occur due to its asymmetry (as seen through the energy framework diagrams) and in this particular study allowing a pyridine nitrogen to form hydrogen bonds of significantly different strengths (8.36 and 18.80 kJ mol^{-1} in (**2**) and 173.40 kJ mol^{-1} in (**3**)) which contributes to the stability of (**3**). Thus, heterosynthons may have greater utility as building blocks in future crystal engineering endeavours due to the variety of interactions they can form because of their member atoms. Future studies in this field will involve performing more charge density studies on the other polymorph of this heterosynthon and other well known synthons with aim of validating the methods used in this paper to evaluate topological properties as discussed above and to also apply the knowledge gained to predict and hopefully create new synthons which can be used to improve the physicochemical of pharmaceutical compounds.

Acknowledgements

DEH and PWG would like to thank The University of Sydney Bridging Support Scheme for funding. JD would like to thank the University of Sydney for an APA scholarship, the Faculty of Pharmacy for research funding and the Sydney Informatics Hub at the University of Sydney for providing access to HPC Artemis. The work was supported by the Danish National Research Foundation (Center for Materials Crystallography, DNRF-93)

References

(1) Springuel, G.; Norberg, B.; Robeyns, K.; Wouters, J.; Leyssens, T., Advances in Pharmaceutical Co-crystal Screening: Effective Co-crystal Screening through Structural Resemblance. *Cryst. Growth Des.* **2012,** 12, (1), 475-484.

(2) Qiao, N.; Li, M.; Schlindwein, W.; Malek, N.; Davies, A.; Trappitt, G., Pharmaceutical cocrystals: An overview. *Int. J. Pharm.* **2011,** 419, (1-2), 1-11.

(3) Schultheiss, N.; Newman, A., Pharmaceutical Cocrystals and Their Physicochemical Properties. *Cryst. Growth Des.* **2009,** 9, (6), 2950-2967.

(4) Aakeroey, C. B.; Salmon, D. J., Building co-crystals with molecular sense and supramolecular sensibility. *CrystEngComm* **2005,** 7, 439-448.

(5) Galek, P. T. A.; Fabian, L.; Motherwell, W. D. S.; Allen, F. H.; Feeder, N., Knowledge-based model of hydrogen-bonding propensity in organic crystals. *Acta Cryst. Sect. B: Struct. Sci., Cryst. Eng. Mater.,* **2007,** 63, (5), 768-782.

(6) Shattock, T. R.; Arora, K. K.; Vishweshwar, P.; Zaworotko, M. J., Hierarchy of Supramolecular Synthons: Persistent Carboxylic Acid···Pyridine Hydrogen Bonds in Cocrystals That also Contain a Hydroxyl Moiety. *Cryst. Growth Des.* **2008,** 8, (12), 4533-4545.

(7) Wood, P. A.; Feeder, N.; Furlow, M.; Galek, P. T. A.; Groom, C. R.; Pidcock, E., Knowledge-based approaches to co-crystal design. *CrystEngComm* **2014,** 16, (26), 5839-5848.

(8) Etter, M. C., Encoding and decoding hydrogen-bond patterns of organic compounds. *Acc. Chem. Res.* **1990,** 23, (4), 120-6.

(9) Etter, M. C., Hydrogen bonds as design elements in organic chemistry. *J. Phys. Chem.* **1991,** 95, (12), 4601-10.

(10) Mukherjee, A.; Desiraju, G. R., Synthon polymorphism and pseudopolymorphism in co-crystals. The 4, 4′-bipyridine–4-hydroxybenzoic acid structural landscape. *Chem. Commun. (Cambridge, U. K.)* **2011,** 47, (14), 4090-4092.

(11) Farrugia, L. J., ORTEP-3 for Windows-a version of ORTEP-III with a Graphical User Interface (GUI)., *J. Appl. Cryst.* **1997,** 30, (5), 565-565.

(12) Du, J. J.; Váradi, L.; Tan, J.; Zhao, Y.; Groundwater, P. W.; Platts, J. A.; Hibbs, D. E., Experimental and theoretical charge density distribution in Pigment Yellow 101. *Phys. Chem. Chem. Phys.* **2015,** 17, (6), 4677-4686.

(13) Du, J. J.; Váradi, L.; Williams, P. A.; Groundwater, P. W.; Overgaard, J.; Platts, J. A.; Hibbs, D. E., An analysis of the experimental and theoretical charge density distributions of the piroxicam-saccharin co-crystal and its constituents. *RSC Adv.*, **2016**, 6, 81578-81590.

(14) Lai, F.; Du, J. J.; Williams, P. A.; Váradi, L.; Baker, D.; Groundwater, P. W.; Overgaard, J.; Platts, J. A.; Hibbs, D. E., A comparison of the experimental and theoretical charge density distributions in two polymorphic modifications of piroxicam. *Phys. Chem. Chem. Phys.* **2016,** 18, (41), 28802-28818.

(15) Boag, N. M.; Coward, K. M.; Jones, A. C.; Pemble, M. E.; Thompson, J. R., 4,4'-Bipyridyl at 203K. *Acta Cryst. Sect. C: Struct. Chem.*, **1999,** 55, (4), 672-674.

(16) Heath, E. A.; Singh, P.; Ebisuzaki, Y., Structure of p-hydroxybenzoic acid and p-hydroxybenzoic acid-acetone complex (2/1). *Acta Cryst. Sect. C: Struct. Chem.* **1992,** 48, (11), 1960-1965.

(17) Oswald, I. D. H.; Allan, D. R.; McGregor, P. A.; Motherwell, W. D. S.; Parsons, S.; Pulham, C. R., The formation of paracetamol (acetaminophen) adducts with hydrogen-bond acceptors. *Acta Cryst. Sect. B: Struct. Sci., Cryst. Eng. Mater.* **2002,** 58, (6), 1057-1066.

(18) Alkorta, I.; Elguero, J.; Roussel, C., A theoretical study of the conformation, basicity and NMR properties of 2, 2′-, 3, 3′-and 4, 4′-bipyridines and their conjugated acids. *Comp. Theor. Chem.* **2011,** 966, (1), 334-339.

(19) Macrae, C. F.; Bruno, I. J.; Chisholm, J. A.; Edgington, P. R.; McCabe, P.; Pidcock, E.; Rodriguez-Monge, L.; Taylor, R.; Streek, J. v.; Wood, P. A., Mercury CSD 2.0–new features for the visualization and investigation of crystal structures. *J. Appl. Cryst.,* **2008,** 41, (2), 466-470.
(20) Release, S., 3: Maestro, version 11.2. *Schrödinger, LLC, New York, NY* **2017**.
(21) Bader, R. F. W., *Atoms in Molecules: A Quantum Theory*. ed.; Oxford Univ. Press: 1994; p 454 pp.
(22) Coppens, P., *X-Ray Charge Densities and Chemical Bonding* ed.; Oxford University Press New York, 1997.
(23) Koch, U.; Popelier, P. L. A., Characterization of C-H-O Hydrogen Bonds on the Basis of the Charge Density. *J. Phys. Chem.,* **1995,** 99, (24), 9747-9754.
(24) Abramov, Y., On the Possibility of Kinetic Energy Density Evaluation from the Experimental Electron-Density Distribution. *Acta Cryst. Sect. A: Found. Adv.,* **1997,** 53, (3), 264-272.
(25) Espinosa, E.; Souhassou, M.; Lachekar, H.; Lecomte, C., Topological analysis of the electron density in hydrogen bonds. *Acta Cryst. Sect. B: Struct. Sci., Cryst. Eng. Mater.,* **1999,** 55, (4), 563-572.
(26) Ziólkowski, M.; Grabowski, S. J.; Leszczynski, J., Cooperativity in hydrogen-bonded interactions: ab initio and "atoms in molecules" analyses. *J. Phys. Chem. A* **2006,** 110, (20), 6514-6521.
(27) Steiner, T., The hydrogen bond in the solid state. *Angew. Chem. Int. Ed.* **2002,** 41, (1), 48-76.
(28) Wolff, S.; Grimwood, D.; McKinnon, J.; Turner, M.; Jayatilaka, D.; Spackman, M., Crystal Explorer ver. 3.1. *University of Western Australia, Perth, Australia* **2013**.
(29) Turner, M.; McKinnon, J.; Wolff, S.; Grimwood, D.; Spackman, P.; Jayatilaka, D.; Spackman, M., CrystalExplorer17. *University of Western Australia* **2017**.
(30) Surov, A. O.; Simagina, A. A.; Manin, N. G.; Kuzmina, L. G.; Churakov, A. V.; Perlovich, G. L., Fenamate Cocrystals with 4,4'-Bipyridine: Structural and Thermodynamic Aspects. *Cryst. Growth Des.* **2015,** 15, (1), 228-238.
(31) Surov, A. O.; Solanko, K. A.; Bond, A. D.; Bauer-Brandl, A.; Perlovich, G. L., Polymorphism of felodipine co-crystals with 4,4[prime or minute]-bipyridine. *CrystEngComm* **2014,** 16, (29), 6603-6611.
(32) Hubschle, C. B.; Luger, P., MolIso - a program for colour-mapped iso-surfaces. *J. Appl. Cryst.,* **2006,** 39, (6), 901-904.
(33) Volkov, A.; Macchi, P.; Farrugia, L. J.; Gatti, C.; Mallinson, P.; Richter, T.; Koritsanszky, T. *XD2006- a computer program for multipole refinement, topological analysis of charge densities and evaluation of intermolecular energies from experimental or theoretical structure factors*, 2006.
(34) Gavezzotti, A., Calculation of lattice energies of organic crystals: the PIXEL integration method in comparison with more traditional methods. In *Z. Kristallogr. - Cryst. Mater.,* 2005; 220, 499-510
(35) Spackman, M. A., A simple quantitative model of hydrogen bonding. *J. Chem. Phys.,* **1986,** 85, (11), 6587-6601.
(36) Volkov, A.; Coppens, P., Calculation of electrostatic interaction energies in molecular dimers from atomic multipole moments obtained by different methods of electron density partitioning. *J. Comp. Chem.,* **2004,** 25, (7), 921-934.
(37) Volkov, A.; Koritsanszky, T.; Coppens, P., Combination of the exact potential and multipole methods (EP/MM) for evaluation of intermolecular electrostatic interaction energies with pseudoatom representation of molecular electron densities. *Chem. Phys. Letts.,* **2004,** 391, (1–3), 170-175.
(38) Volkov, A.; Li, X.; Koritsanszky, T.; Coppens, P., Ab Initio Quality Electrostatic Atomic and Molecular Properties Including Intermolecular Energies from a Transferable Theoretical Pseudoatom Databank. *J. Phys. Chem. A.,* **2004,** 108, (19), 4283-4300.
(39) Spackman, M. A., Atom–atom potentials via electron gas theory. *J. Chem. Phys.* **1986,** 85, (11), 6579-6586.

(40) Gavezzotti, A., Non-conventional bonding between organic molecules. The 'halogen bond' in crystalline systems. *Mol. Phys.* **2008,** 106, (12-13), 1473-1485.
(41) Spackman, M. A., How Reliable Are Intermolecular Interaction Energies Estimated from Topological Analysis of Experimental Electron Densities? *Cryst. Growth Des.,* **2015,** 15, (11), 5624-5628.
(42) Frisch, M. J.; Trucks, G. W.; Schlegel, H. B.; Scuseria, G. E.; Robb, M. A.; Cheeseman, J. R.; Scalmani, G.; Barone, V.; Mennucci, B.; Petersson, G. A.; Nakatsuji, H.; Caricato, M.; Li, X.; Hratchian, H. P.; Izmaylov, A. F.; Bloino, J.; Zheng, G.; Sonnenberg, J. L.; Hada, M.; Ehara, M.; Toyota, K.; Fukuda, R.; Hasegawa, J.; Ishida, M.; Nakajima, T.; Honda, Y.; Kitao, O.; Nakai, H.; Vreven, T.; Montgomery, J. A., Jr.; Peralta, J. E.; Ogliaro, F.; Bearpark, M.; Heyd, J. J.; Brothers, E.; Kudin, K. N.; Staroverov, V. N.; Kobayashi, R.; Normand, J.; Raghavachari, K.; Rendell, A.; Burant, J. C.; Iyengar, S. S.; Tomasi, J.; Cossi, M.; Rega, N.; Millam, N. J.; Klene, M.; Knox, J. E.; Cross, J. B.; Bakken, V.; Adamo, C.; Jaramillo, J.; Gomperts, R.; Stratmann, R. E.; Yazyev, O.; Austin, A. J.; Cammi, R.; Pomelli, C.; Ochterski, J. W.; Martin, R. L.; Morokuma, K.; Zakrzewski, V. G.; Voth, G. A.; Salvador, P.; Dannenberg, J. J.; Dapprich, S.; Daniels, A. D.; Farkas, Ö.; Foresman, J. B.; Ortiz, J. V.; Cioslowski, J.; Fox, D. J. *Gaussian09*, 2006.
(43) Jayatilaka, D.; Grimwood, D. J. In *Tonto: a fortran based object-oriented system for quantum chemistry and crystallography*, International Conference on Computational Science, **2003**, 142-151.